Available online at www.sciencedirect.com

ScienceDirect

Underground Space 3 (2018) 252–267

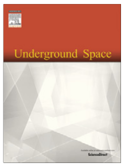

www.elsevier.com/locate/undsp

Multiscale structural analysis inspired by exceptional load cases concerning the immersed tunnel of the Hong Kong-Zhuhai-Macao Bridge

Hui Wang [a,b], Eva Binder [a,b], Herbert Mang [a,b], Yong Yuan [b], Bernhard Pichler [a,*]

[a] *Institute for Mechanics of Materials and Structures, TU Wien – Vienna University of Technology, Karlsplatz 13/202, A-1040 Vienna, Austria*
[b] *College of Civil Engineering, Tongji University, Shanghai, China*

Received 30 November 2017; received in revised form 14 February 2018; accepted 26 February 2018
Available online 4 April 2018

Abstract

This paper contains an assessment of the added value of multiscale material models for concrete in the context of macroscopic structural analysis of (steel-reinforced) concrete structures. Two examples are discussed. They are inspired by the possibility of car accidents inside the immersed tunnel of the Hong Kong-Zhuhai-Macao Bridge (HZMB). The first example deals with vehicles crashing into the tunnel wall. The high-dynamic strengthening effect of concrete is studied based on an engineering mechanics model. The *structural* nature of the dynamic strength increase factor (*DIF*) is demonstrated by means of high-dynamic strength values measured on mortar cylinders of different size. Furthermore, the evolution of the *DIF* as a function of hardening of concrete at material ages beyond 28 days is studied. A validated multiscale model for concrete renders a customized analysis for the specific concrete used for the aforementioned tunnel possible. It is found that the *DIF decreases* with progressive hardening of concrete at material ages beyond 28 days. The second example is inspired by tunnel fires as may happen after car accidents. The study refers to thermal stresses in steel-reinforced concrete beams subjected to sudden heating. The thermal expansion coefficient of the concrete of the tunnel is quantified by means of a multiscale model. It is used as input for linear thermo-mechanical Finite-Element simulations of steel-reinforced concrete beams. The essential macroscopic simulation results are temperature distributions and associated stress fields. They are employed for top-down quantification of microscopic stress states inside the cement paste and the aggregates. This allows for quantifying two sources of microstructural stress fluctuations: (i) the macro-to-micro stress concentration and (ii) the mismatch of microscopic thermal expansion coefficients. In both examples, the multiscale models for concrete have increased the informative content of the structural simulations.

Keywords: Concrete linings; High-dynamic strength; Thermal stresses

1 Introduction

The Hong Kong-Zhuhai-Macao Bridge (HZMB), connecting Hong Kong on the east bank of the Pearl River with Macao and Zhuhai on its west bank, is around 35.6 km long. For shipping, the bridge is interrupted by a 5.7 km long immersed tunnel below the bottom of the sea, which is the research focus of this study (Fig. 1). The tunnel is designed to serve for a period of 120 years, during which exceptional loading events such as traffic accidents may happen. This includes the possibility of cars crashing into one of the tunnel walls, resulting in high-dynamic compressive loading of concrete. Such accidents may be followed by tunnel fires, resulting in thermal loading of the concrete lining. This sets the scene for the present study. It aims to assess the potential added value that may result from combining macroscopic modes of structural analysis

---

[*] Corresponding author.
E-mail address: Bernhard.Pichler@tuwien.ac.at (B. Pichler).

https://doi.org/10.1016/j.undsp.2018.02.001
2467-9674/

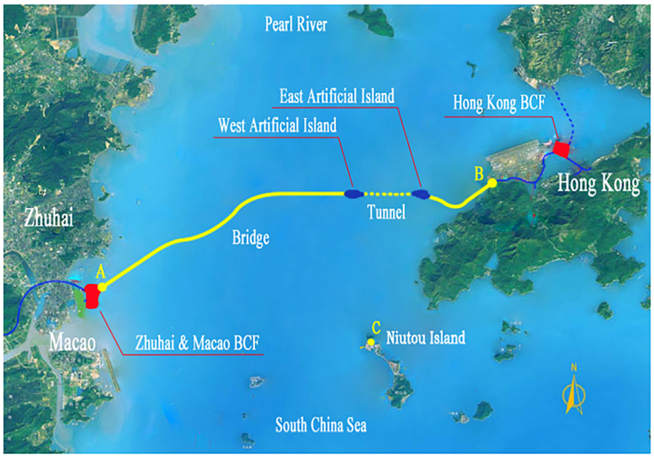

Fig. 1. Course of the Hong Kong-Zhuhai-Macao-Bridge; from Binder et al. (2018).

with multiscale models for concrete. The latter modes provide two types of scale-transitions, referred to as “bottom-up homogenization” and “top-down stress concentration”. They are described in the next two paragraphs.

Bottom-up homogenization allows for quantification of macroscopic properties of concrete, based on the knowledge regarding the microstructural composition of the material. Validated models are nowadays available for the elastic stiffness (Bernard et al., 2003; Hellmich and Mang, 2005), creep behavior (Königsberger et al., 2016; Irfan-ul-Hassan et al., 2017), compressive strength (Königsberger et al., 2018), and thermal expansion coefficients (Wang et al., 2017b, submitted for publication) of concrete. In the present study, bottom-up homogenization of concrete is used to provide *input values* for macroscopic structural analyses.

Top-down stress concentration (Bernard et al., 2003) allows for quantifying the stress states of microstructural constituents, based on the knowledge regarding the macroscopic loading of a representative material volume of concrete (Zaoui, 2002; Dormieux et al., 2006). Methods for such scale transitions are nowadays capable of accounting for thermal eigenstrains (Dvorak, 1992; Pichler and Hellmich, 2010). In the present study, top-down scale transitions are used for *postprocessing* of results from macroscopic structural analyses.

The potential added value resulting from the use of multiscale material models for concrete in the context of macroscopic structural analysis of (steel-reinforced) concrete structures is assessed as follows. Multiscale models for the elastic stiffness, compressive strength, and thermal expansion coefficient of concrete are employed for two types of structural analyses, inspired by exceptional load cases of the immersed tunnel of the HZMB. The first type of structural analysis deals with impact problems and refers to the high-dynamic strength of the concrete used for the tunnel. The second type of structural analysis is inspired by tunnel fires and refers to multiscale analysis of stress states in steel-reinforced concrete beams subjected to sudden heating. An introduction to these two topics follows in the next two paragraphs.

Quasi-static and high-dynamic testing of cementitious materials indicates that the strength of the tested specimens increases with increasing loading rate. The strengthening effect is significant in the high-dynamic loading regime, where the strain rates are larger than $10\,\mathrm{s}^{-1}$ (see, e.g. Tai, 2009). This effect is quantified, based on the dynamic strength increase factor *DIF*. It is defined as the ratio of (i) the dynamic strength, f_{dyn}, which is a function of the strain rate $\dot{\varepsilon}$, and (ii) the quasi-static strength, f_{stat}, which is standardly measured, using a strain rate on the order of magnitude of $10^{-5}\,\mathrm{s}^{-1}$. Thus,

$$DIF = \frac{f_{dyn}}{f_{stat}}. \tag{1}$$

In Eq. (1), f_{dyn} stands either for a *measured* value of the dynamic strength of an empirically tested *specific specimen*, or for a *model-predicted* value that refers to the *statistical population* of infinitely many samples that could, at least theoretically, be produced and tested. Because strength tests are destructive, it is impossible to determine both the quasi-static *and* the high-dynamic strength of an individual specimen. Therefore, f_{stat} in Eq. (1) always stands for a property of the *statistical population* of infinitely many samples. The present analysis makes use of the following formula by Fischer et al. (2014) for the dynamic strength:

$$f_{dyn} = f_{stat} + E\,\dot{\varepsilon}\,\frac{\ell_c}{\sqrt{\mu/\rho}}, \tag{2}$$

where E, ℓ_c, μ, and ρ represent Young’s modulus, the characteristic crack propagation length, the shear modulus, and the mass density, respectively. As for the present study, Eqs. (1) and (2) provide the motivation for two types of analysis. On the one hand, Eqs. (1) and (2) suggest that the *DIF* depends, via ℓ_c, on the size of a tested specimen. This dependence of the *DIF* will be assessed, based on experimental data taken from Zhang et al. (2009), who tested two groups of mortar specimens of *different size*. On the other hand, Eqs. (1) and (2) suggest that the *DIF* depends, via the expression $E/(f_{stat}\sqrt{\mu})$, on the quasi-static strength and on the stiffness properties of concrete. Eqs. (1) and (2) will be applied to the concrete used for the aforementioned immersed tunnel, in order to study the evolution of the *DIF* at concrete ages beyond 28 days. This analysis accounts for the fact that hardening of concrete continues progressively rather than stops abruptly at a material age of 28 days. The evolution of the elastic stiffness and the quasi-static compressive strength will be quantified according to (i) the recommendations of the *FIB* Model Code 2010 Taerwe and Matthys (2013) and (ii) the multiscale model by Königsberger et al. (2018).

Imposing a sudden temperature increase on a steel-reinforced concrete structure results in thermal stresses. Corresponding three-dimensional Finite Element analyses are nowadays typically limited to *macroscopic* numerical simulation (Kodur and Dwaikat, 2008; Bary et al., 2012; Feist et al., 2009; Bangert et al., 2003), while *multiscale* analysis is typically limited to two-dimensional simulations of plain concrete cubes (Zhao et al., 2014; Fu et al., 2004a,b, 2007). The focus of the second part of the present paper is on three-dimensional analysis of macroscopic *and* microscopic stress states in steel-reinforced concrete beams, subjected to sudden heating of their bottom surfaces. The structural dimensions of the beams and their reinforcement are equal to corresponding properties of the overhead-slabs of the segments of the immersed tunnel of the HZMB. The elastic stiffness and the thermal expansion coefficient of the concrete of the immersed tunnel are quantified, using the multiscale models by Königsberger et al. (2018) and Wang et al. (2017b, submitted for publication). In the context of postprocessing of the structural analyses, both the obtained temperature field and the computed macroscopic stress fields are used as input for *top-down quantification of the average stress states* experienced by the cement paste and the aggregates constituting the analyzed concrete. This allows for quantifying heating-induced stress fluctuations at the microstructure of concrete.

The present paper is structured as follows. Section 2 refers to the construction sequence of the immersed tunnel of the HZMB, the layout of its precast reinforced concrete segments and their steel reinforcements, and the composition of the used concrete. Section 3 deals with the analysis of the high-dynamic strengthening effect. Section 4 is concerned with multiscale thermo-mechanical analysis. Section 5 contains the conclusions drawn from the presented analyses.

2 Immersed tunnel of the Hong Kong-Zhuhai-Macao Bridge

The immersed tunnel of the HZMB consists of 33 elements which are produced on Niutou Island, 12 km south of the site (marked with “C” in Fig. 1). Each element consists of eight segments made of steel-reinforced concrete. They are produced sequentially at the finished-part plant. The segments are connected by prestressed cables set in concrete. The cross-sections at the beginning and at the end of a completed element are sealed by temporary steel bulk-heads so that the elements can float. Additionally, a sealing ring is mounted onto the outside edges of the initial cross-section. Having reached the site, the elements are immersed into a trench at the bottom of the sea, whereby the maximum water depth amounts to almost 45 m (Hu et al., 2015). With the help of ropes, the immersion process is controlled from pontoons. The new element is maneuvered to the end of the already existing part of the immersed tunnel. By means of hydraulic cylinders, the new element is moved to the previously immersed neighboring element until the two elements are in full contact along the sealing ring. Subsequently, the water inside the sealing ring and the two steel bulk-heads is pumped out. The remaining water pressure at the end cross-section of the new element moves this element more closely to the previously built-in neighboring element, thus exerting compression on the sealing ring. This results in a permanent sealing of the immersed tunnel. A further sealing element is installed in the pumped-out region between the two neighboring elements. After a pressure test concerning the tightness of the two sealing elements, the hydraulic cylinders and the steel bulk-heads are finally dismantled. After the construction of the tunnel, the elements are covered with backfill material, such that the height of the overburden amounts up to 23 m (Hu et al., 2015).

The segments of the immersed tunnel are steel-reinforced concrete structures of impressive dimensions. The thickness of the overhead-slab, for instance, is 1500 mm. Its cross-section contains four layers of rebars. As shown in Fig. 2, three layers are close to the inner surface, and one layer is close to the top surface. The diameters of the rebars in the lowermost layer are 32 mm. In the next two layers, they are 36 mm, and in the uppermost layer, they are 40 mm. The concrete, in turn, consists of aggregates from three grading fractions, water, and a binder that is a mixture of Portland cement, fly ash, and slag (Table 1). Young’s modulus and the compressive strength of plain concrete were determined at material ages amounting to 3, 7, and 28 days (Table 2).

3 Multiscale analysis of the structural nature of high-dynamic strengthening of concrete

The expression for the *DIF*, resulting from the combination of Eqs. (1) and (2), is based on the following modeling ideas of Fischer et al. (2014). Cracking of concrete starts, also under high-dynamic loading, once the quasi-static strength is reached. The cracks propagate at a speed that is approximately equal to the shear wave velocity. During crack propagation, it is possible to further increase the loading of the specimen. The high-dynamic strength is reached at the time instant when the first crack has propagated along the length ℓ_c, splitting the specimen.

Considerable uncertainties are associated with the *DIF*, because it is defined as the dynamic strength divided by the quasi-static strength, see Eq. (1), and both strength values are statistical quantities.

- In order to account for the statistical scatter of the quasi-static strength, Binder et al. (2017) derived expressions for the 5% and 95% quantiles of the compressive strength, which are consistent with the semi-probabilistic design philosophy of the Eurocode 2 (European Committee for Standardization, 2011). Thus, the quasi-static strength, f_{stat}, in Eq. (1) may be set equal to its 5% quantile, expected value, or 95% quantile. This will result in an upper limit, the expected value, and a lower limit of the *DIF*, respectively.
- In order to account for the statistical scatter of the dynamic strength, Fischer et al. (2014) considered (i) two extreme cases regarding the position of crack

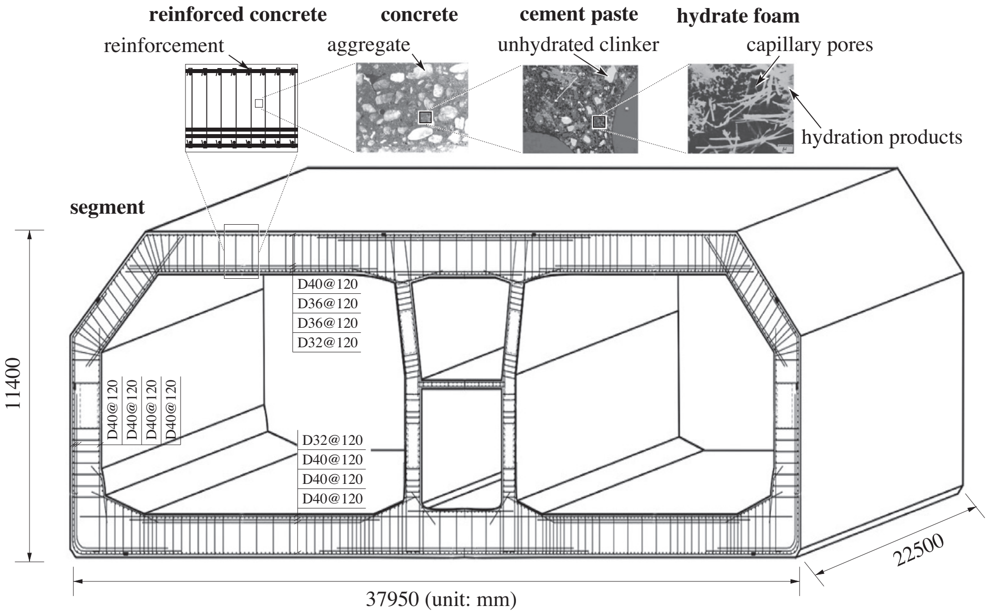

Fig. 2. Hierarchical organization of the steel-reinforced segments of the immersed tunnel of the Hong Kong-Zhuhai-Macao Bridge; the micrographs are taken from Walker et al. (2006) and Chatterji and Jeffery (1966), respectively.

Table 1
Composition for the concrete used for the steel-reinforced segments of the immersed tunnel of the Hong Kong-Zhuhai-Macao Bridge, with an initial water-to-binder mass ratio w/b, amounting to 0.35, and a mass density of 2389 kg/m^3.

Raw materials	Dosages [kg/m^3]
Binder	420
Water	147
Aggregates	1822

Table 2
Experimentally determined Young's moduli and compressive strength values of the concrete used for the steel-reinforced concrete segments of the immersed tunnel of the Hong Kong-Zhuhai-Macao Bridge.

Age [day]	Young's modulus [GPa]	Compressive strength [MPa]
3	32.8	30.4
7	37.5	42.1
28	43.3	66.5

nucleation, and (ii) two corresponding values of the related crack propagation length ℓ_c. Thereby, they considered crack propagation in the loading direction ("axial splitting"), as observed in their experiments. The first extreme scenario refers to crack nucleation right at one of the interfaces between the specimen and the load application system. The crack tip has to propagate along the entire height h of the specimen. The second extreme scenario refers to crack nucleation in the middle of the specimen. Both crack tips have to propagate along half of the height of the specimen in order to split the specimen. Thus, the crack propagation length, ℓ_c, in Eq. (2) may either be set to $1.0h$ or $0.5h$. This will result in a lower limit and an upper limit of the *DIF*, respectively.

Notably, the modeling idea of Fischer et al. (2014) is consistent with multiple cracking and fragmented failure patterns, because high-dynamic strengthening is related to an increase in the external loading *during* the propagation of the crack that nucleated at the weakest spot. Multiple cracking, in turn, could also lead to crack coalescence. Thus, the effective crack propagation length ℓ_c could be, strictly speaking, even smaller than $0.5h$.

3.1 Macroscopic assessment of the predictive capabilities of the DIF model by Fischer et al. (2014)

The described *DIF* model is capable of providing blind predictions, because all material properties in Eqs. (1) and (2) are accessible by means of quasi-static testing. As for cement paste and concrete, respectively, the model was applied to test series by Fischer et al. (2014) and by Kühn et al. (2016). The input quantities required for the application of Eqs. (1) and (2) and the test results from high-dynamic strength testing are listed in Table 3. The model-predictions agree well with the experimental data (Fig. 3). The two solid lines in Fig. 3(a) refer to model predictions obtained with the expected value of f_{stat} and with ℓ_c values taken from the interval $[0.5h; 1.0h]$. The upper (lower) boundary of the adjacent yellow areas in Fig. 3(a) refers to consideration of (i) the 5% quantile (95% quantile) of f_{stat} in the denominator of the expression for the *DIF*, given in Eq. (1), and (ii) the *expected value* of f_{stat} as well as $\ell_c = 1.0h$ ($\ell_c = 0.5h$) in the expression for f_{dyn}, given in Eq. (2). This approach implies that the uncertainty regarding the *high-dynamic* strength is exclusively related to the uncertainty regarding the position of crack nucleation. The two described choices regarding the values of f_{stat} also

Table 3
High-dynamic strength values from (a) Fischer et al. (2014), who tested cement paste specimens with $f_{stat} = 48.16$ MPa, $E = 14.24$ GPa, $\mu = 5.53$ GPa, $h = 6.6$ mm, and $\rho = 1593$ kg/m^3, as well as (b) Kühn et al. (2016), who tested concrete specimens with $f_{stat} = 25.1$ MPa, $E = 32$ GPa, $\mu = 13.3$ GPa, $h = 80$ mm, and $\rho = 2400$ kg/m^3.

$\dot{\varepsilon}$ [s^{-1}]	f_{dyn} [MPa]	$\dot{\varepsilon}$ [s^{-1}]	f_{dyn} [MPa]
	(a)		
700	74.15	1900	132.73
200	42.01	2100	164.39
500	74.41	2100	156.36
500	48.60	2100	133.73
500	65.40	2100	152.64
5000	114.26	1900	143.78

$\dot{\varepsilon}$ [s^{-1}]	f_{dyn} [MPa]
(b)	
$8.6 \cdot 10^{-6}$	25.1
136.6	95.1
150.1	104.2
185.5	119.2
190.0	125.7
202.7	142.5

explain why the lower yellow area in Fig. 3(a) comprises values of the *DIF* that are smaller than 1. As for the analyzed concrete, it is noteworthy that Kühn et al. (2016) provided photographs of the fragments of the specimens after testing, suggesting that the cracks propagated along a length equal to one half of the specimen height. Thus, $\ell_c = 0.5h$, see also (Binder et al., 2018). This knowledge limits the uncertainty to the statistical scatter of f_{stat} in the denominator of Eq. (1), illustrated as yellow areas in Fig. 3(b).

Eqs. (1) and (2) suggest that the *DIF* depends, via ℓ_c, on the size of the tested specimen. In order to assess this aspect, it is desirable to apply the *DIF* model to a test series including specimens of *different sizes*. Zhang et al. (2009) have tested two groups of cylindrical mortar specimens using the *the same mortar* but *different specimen heights*: $h = 18$ mm and $h = 25$ mm, respectively. Thus, the test results allow for a quantitative assessment of the ℓ_c-dependence of the *DIF*, as suggested by the combination of Eqs. (1) and (2). The input quantities required for the application of Eqs. (1) and (2) and the test results from high-dynamic strength testing are listed in Table 4. Model-predictions for both specimen sizes agree well with the experimental data, see Fig. 4. This agreement further supports the the usefulness of the employed *DIF* model and provides the motivation for applying it to the concrete used for the HZMB.

3.2 Multiscale analysis regarding the influence of concrete-hardening on the evolution of the DIF

Current design standards use mechanical properties of concrete 28 days after production as the basis for regulations concerning the layout of steel-reinforced concrete structures. However, the chemical hardening reaction between the binder and water continues at material ages beyond 28 days. This provides the motivation to analyze the corresponding evolution of the *DIF*. According to Eqs. (1) and (2), this study requires quantitative estimates of the evolutions of the quasi-static strength, Young's modulus, and the shear modulus. These estimates are computed, using a recently developed multiscale model for concrete.

In the multiscale model for concrete by Königsberger et al. (2018), the microstructure of concrete is considered as a hierarchical scheme of three representative volume elements (RVEs), see Fig. 5 and compare with the micrographs of Fig. 2. Centimeter-sized RVEs of concrete consist of spherical aggregates that are embedded in a cement paste matrix (Fig. 5(a)). Submillimeter-sized RVEs of cement paste consist of spherical binder grains that are embedded in a hydrate foam matrix (Fig. 5(b)). Micrometer-sized RVEs of the hydrate foam consist of spherical capillary pores and of needle-shaped hydrates that are uniformly oriented in all space directions (Fig. 5(c)).

The evolutions of the elastic stiffness and the uniaxial compressive strength of concrete are essentially related (i)

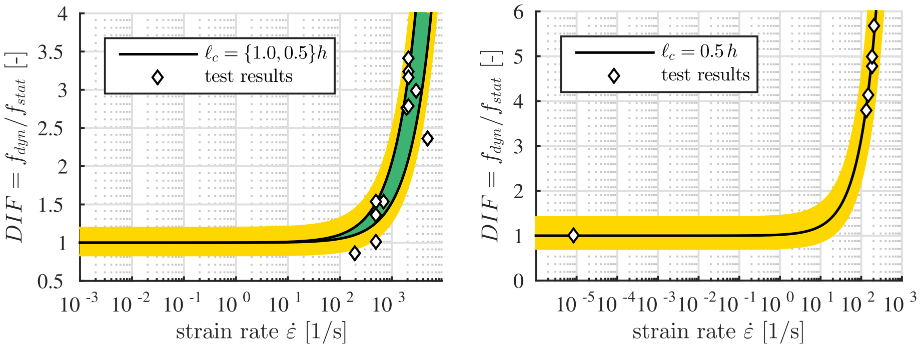

(a) (b)

Fig. 3. Comparison of model-predicted *DIF* values according to Eqs. (1) and (2) with *DIF* values related to the measured high-dynamic strength values listed in Table 3: (a) cement pastes tested by Fischer et al. (2014) and (b) concrete tested by Kühn et al. (2016); after Fischer et al. (2014) and Binder et al. (2018); the green area refers to the uncertainty regarding the high-dynamic strength, resulting from the uncertainty regarding the position of crack nucleation, and the yellow areas to additional consideration of the uncertainty regarding the quasi-static strength in the denominator of Eq. (1).

Table 4
High-dynamic strength values from Zhang et al. (2009), who tested mortar specimens with $f_{stat} = 51$ MPa, $E = 23.1$ GPa, $\mu = 9.71$ GPa, $\rho = 2116$ kg/m^3, and (a) $h = 18$ mm and (b) $h = 25$ mm.

$\dot{\varepsilon}$ [s^{-1}]	f_{dyn} [MPa]	$\dot{\varepsilon}$ [s^{-1}]	f_{dyn} [MPa]
	(a)		
49	70.56	205	86.57
71	73.82	295	90.44
85	74.75	338	96.52
131	75.11	346	98.16
153	75.69	323	99.45
184	79.67	330	101.67
220	81.66	453	109.04
$\dot{\varepsilon}$ [s^{-1}]	f_{dyn} [MPa]	$\dot{\varepsilon}$ [s^{-1}]	f_{dyn} [MPa]
	(b)		
37	64.45	126	79.14
69	71.22	165	82.03
76	71.47	192	88.80
86	75.02	165	93.34
89	72.13	229	93.75
126	76.01	261	98.62
153	77.00		

to the material *constants* of the solid constituents of concrete: hydrates, binder, and aggregates (Table 5) and (ii) to the hydration-induced *evolutions* of their volume fractions. Notably, the needle-shaped hydrates represent the “glue” of concrete. Therefore, their stiffness *constants* (Table 5) and strength *constants*, i.e. their cohesion, c_{hyd}, and angle of internal friction, φ_{hyd}, (Sarris and Constantinides, 2013)

$$c_{hyd} = 50\ \text{MPa}, \quad \varphi_{hyd} = 12^\circ, \tag{3}$$

are governing the macroscopic stiffness and strength properties of the concretes. The *evolution* of the latter is a consequence of the chemical reaction between the binder and water. In more detail, binder grains and capillary porewater are progressively consumed, while needle-shaped hydrates are produced. Hydration models, such as the ones by Powers and Brownyard (1946), Acker (2001), and Hansen (1986), describe the evolution of the phase volume fractions as a function of the degree of hydration. Thermochemical models, such as the chemical affinity concept (Ulm and Coussy, 1995), are used to describe the temporal evolution of the degree of hydration, considering that the faster the exothermic hydration process proceeds, the higher the curing temperature will be. Unfortunately, the advancement of the degree of hydration of the concrete used for the immersed tunnel of the HZMB is unknown. Still, the applicability of the described multiscale model can be checked quantitatively, based on the following correlation analysis of the evolution of the stiffness and the strength.

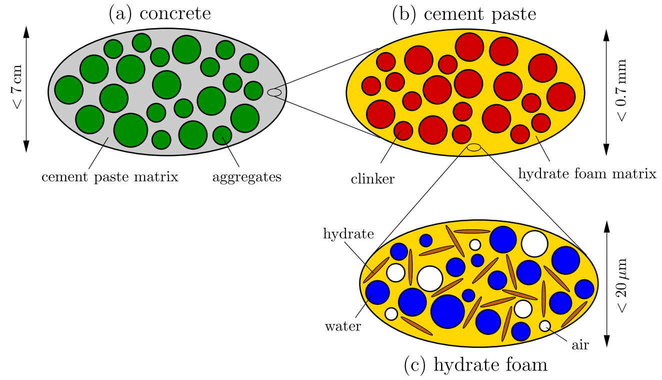

Fig. 5. Representation of the microstructure of concrete by a hierarchical scheme of three scale-separated RVEs (“material organogram”). The two-dimensional sketches refer to three-dimensional RVEs; after Königsberger et al. (2018).

Table 5
Isotropic elastic stiffness constants of the solid constituents of concrete.

	Hydrates	Binder	Quartz aggregates
Young’s modulus E [GPa]	29.2	139.9	60.0
Shear modulus μ [GPa]	11.8	53.8	23.0

The described multiscale model is evaluated for the concrete used for the immersed tunnel of the HZMB,

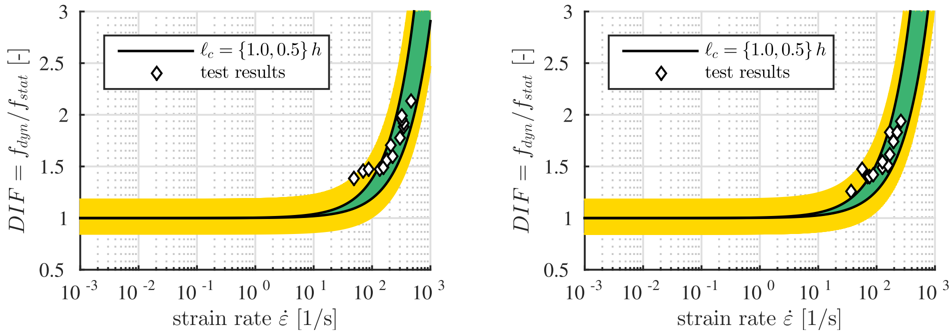

(a) (b)

Fig. 4. Comparison of model-predicted *DIF* values according to Eqs. (1) and (2) with measured *DIF* values from Zhang et al. (2009), see Table 4, referring to mortar cylinders with heights (a) $h = 18$ mm and (b) $h = 25$ mm; the green areas refer to the uncertainty regarding the high-dynamic strength, resulting from the uncertainty regarding the position of crack nucleation, and the yellow areas refer to additional consideration of the uncertainty regarding the quasi-static strength in the denominator of Eq. (1).

considering progressively increasing values of the hydration degree. The essential input values for these computations are the initial composition of the analyzed concrete (Table 1), the stiffness constants of the solid constituents of the concrete (Table 5), and the strength properties of the hydrates (see Eq. (3)). The obtained predictions concerning Young's modulus and the uniaxial compressive strength are illustrated in a parametric diagram, using the hydration degree as the parameter. Notably, the model-predicted evolution of the stiffness-strength relation is in good qualitative and quantitative agreement with the available experimental data (see the data points and the solid line in Fig. 6(a)). This suggests that the multiscale model delivers a reliable correlation between stiffness and strength values, even for untested scenarios (see, e.g. the solid line in Fig. 6(b) for the model-predicted evolution of the shear modulus). Unfortunately, the reaction kinetics of the binder used for the concrete is unknown. It is, therefore, impossible to assign an evolution of the material age of concrete to the model-predicted evolutions of stiffness and strength.

In order to assess the added value provided by the employed multiscale model, it is interesting to compare the performance of the multiscale model with that of the *FIB* Model Code 2010 (Taerwe & Matthys, 2013). Based on the stiffness and strength values of concrete, measured 28 days after production (Table 2), the Model Code suggests the following formulae for quantification of the evolution of the stiffness and the strength:

$$E(t) = 43.3\ \text{GPa} \cdot \left\{ \exp\left[0.25\left(1 - \sqrt{\frac{28\ \text{days}}{t}} \right) \right] \right\}^{0.5}, \qquad (4)$$

$$f_{stat}(t) = 66.5\ \text{MPa} \cdot \exp\left[0.25\left(1 - \sqrt{\frac{28\ \text{days}}{t}} \right) \right], \qquad (5)$$

see the dashed line in Fig. 6(a). The corresponding evolution of the shear modulus is computed from the standard relation of isotropic elasticity,

$$\mu = \frac{E}{2\,(1+\nu)}, \qquad (6)$$

see the dashed line in Fig. 6(b). In Eq. (6), ν denotes Poisson's ratio of concrete. The Model Code recommends a constant value of 0.2.

The multiscale model by Königsberger et al. (2018) explains that the early-age evolution of the stiffness and the strength of the concrete of the HZMB are significantly better than the recommendations by the Model Code, see Fig. 6(a). Consequently, this multiscale model *does* indeed represent an added value. It provides customized predictions for the specific concrete mix of interest, while the *FIB* Model Code 2010 (Taerwe & Matthys, 2013) provides approximation functions that apply to entire classes of many different concrete mixes.

The satisfactory performance of the multiscale model by Königsberger et al. (2018) provides the motivation to quantify the evolution of the *DIF*, resulting from the increase of the stiffness and of the strength at material ages larger than 28 days. To this end, Eqs. (1) and (2) are evaluated for the 28-days value of f_{stat}, amounting to 66.5 MPa, as well as for the increased values 75.0 MPa, 85.0 MPa, and 95.0 MPa. Corresponding stiffness values are obtained from the multiscale model, see the points marked with + symbols in Fig. 6 and the numerical values listed in Table 6. The mass density of concrete is taken from Table 1. The height of the considered concrete cylinders, h, and the characteristic crack propagation length, ℓ_c, are set equal to 80 mm and 40 mm, respectively, by analogy to the specimens analyzed by Kühn et al. (2016) (Table 3).

The *DIF* values predicted by Eqs. (1) and (2) *decrease* with progressive hardening of concrete at material ages beyond 28 days (Fig. 7(a)). This counterintuitive result is

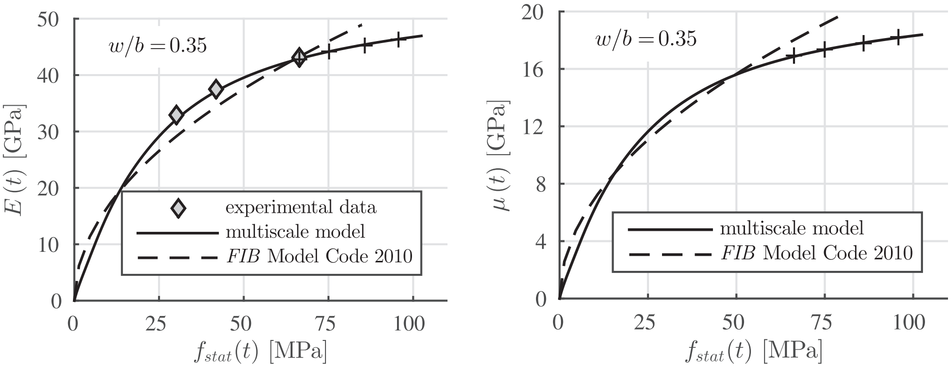

(a) (b)

Fig. 6. Correlation between stiffness and strength of the concrete used for the immersed tunnel of the Hong Kong-Zhuhai-Macao Bridge: experimental data from Table 2, model predictions of the multiscale model by Königsberger et al. (2018), and recommendations of the *FIB* Model Code 2010 (Taerwe & Matthys, 2013): (a) correlation between Young's modulus and the uniaxial compressive strength and (b) correlation between the shear modulus and the uniaxial compressive strength; the + symbols in (a) and (b) label stiffness and strength values that are used for the sensitivity analyses on which Fig. 7 is based; notably, the first + symbol in (a) coincides with the last diamond symbol.

Table 6
Input values for the study concerning the evolution of the *DIF* as a function of hardening of concrete; strength and stiffness values predicted by the multiscale model of Königsberger et al. (2018), applied to the concrete of the immersed tunnel of the Hong Kong-Zhuhai-Macao Bridge.

$f_{stat}(t)$ [MPa]	66.5	75.0	85.0	95.0
$E(t)$ [GPa]	42.9	44.2	45.4	46.4
$\mu(t)$ [GPa]	16.9	17.3	17.8	18.2

related to the expression $E/(f_{stat}\sqrt{\mu})$, see Eqs. (1) and (2). This expression can be re-formulated, based on Eq. (6), as

$$\frac{E}{f_{stat}\sqrt{\mu}} = \frac{\sqrt{E}}{f_{stat}} \frac{1}{\sqrt{2(1+\nu)}}. \tag{7}$$

Considering (i) that ν is practically constant at concrete ages beyond 28 days and (ii) the correlation between E and f_{stat} according to Fig. 6, Eq. (7) clarifies that the *significant* increase in f_{stat} outperforms the accompanying *moderate* increase in the stiffness E, such that $E/(f_{stat}\sqrt{\mu})$ decreases with increasing hardening.

Dynamic strength values f_{dyn} are calculated as the product of the quasi-static strength f_{stat} and the *DIF* values. The dynamic strength values *increase* with progressive hardening of concrete at material ages beyond 28 days, see Fig. 7(b), because the increase in the quasi-static strength f_{stat} outperforms the corresponding decrease in the *DIF*.

It is concluded that the high-dynamic strength of the concrete used for the immersed tunnel of the HZMB increases with progressive hardening of concrete at material ages beyond 28 days. The increase in the high-dynamic strength, however, is less than the corresponding increase in the quasi-static strength, because the increase in the elastic stiffness properties is less pronounced than that in the quasi-static strength. This finding is possible because a validated multiscale model for the stiffness and the strength of concrete was used for macroscopic structural analysis of cylindrical concrete specimens, on the basis of Eqs. (1) and (2).

This completes the first type of multiscale analysis. It is inspired by the possibility of vehicles crashing into the wall of the immersed tunnel. After such accidents, tunnel fires may happen. This is the motivation for the second type of structural analysis reported in this paper.

4 Multiscale analysis of thermal stresses

When steel-reinforced concrete structures are subjected to sudden heating, the material constituents exhibit thermal eigenstrains. The thermal expansion coefficients of steel and concrete are quite similar. Therefore, there is no significant mismatch of the thermal eigenstrains. This is different from the concrete constituents "cement paste" and "aggregates". Concrete aggregates exhibit thermal expansion coefficients ranging between $4 \cdot 10^{-6}/°\text{C}$ and $12 \cdot 10^{-6}/°\text{C}$. They mainly depend on the mineral composition. The cement paste exhibits thermal expansion coefficients ranging between $8 \cdot 10^{-6}/°\text{C}^{-1}$ and $24 \cdot 10^{-6}/°\text{C}$. They mainly depend on the internal relative humidity (Emanuel and Hulsey, 1977). This provides the motivation for bottom-up homogenization of the thermal expansion coefficient of concrete using a one-step homogenization scheme leading from the cement paste matrix and the embedded aggregates to the level of the homogenized concrete (Fig. 5(a)).

4.1 Bottom-up homogenization of the thermal expansion coefficient of the concrete

As for the derivation of the homogenized thermal expansion coefficient of concrete, it is assumed that a representative volume of concrete is subjected to a temperature increase (or decrease) ΔT. The cement paste and the aggregates expand (or contract) according to their specific thermal expansion coefficients, α_{cp} and α_{agg}, respectively. The resulting thermal eigenstrains are

$$\boldsymbol{\varepsilon}_k^e = \alpha_k \Delta T \,\mathbf{1}, \quad k \in [cp, agg], \tag{8}$$

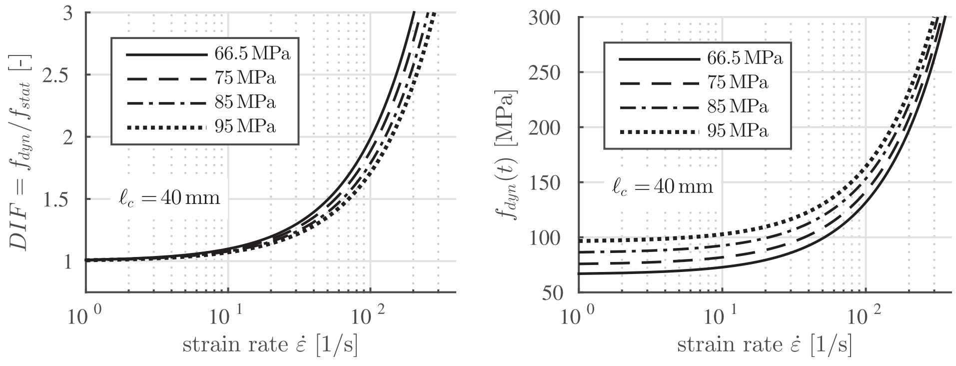

(a) (b)

Fig. 7. Model-predicted evolution of the *DIF* for four different stages of concrete hardening for material ages greater than 28 days: (a) *DIF* values according to Eqs. (1) and (2), see also Table 6 and consider $\ell_c = 40$ mm and $\rho = 2389$ kg/m^3, and (b) dynamic strength $f_{dyn} = f_{stat}\,DIF$.

with **1** standing for the second-order unity tensor. Considering elastic material behavior, the macroscopic constitutive relation of the homogenized concrete is the generalized Hooke's law. The latter relates the macroscopic stress tensor $\boldsymbol{\Sigma}_{con}$ to the difference between the macroscopic strain tensor $\mathbf{E}_{con}$ and the macroscopic eigenstrain tensor $\mathbf{E}^{e}_{con}$, based on the homogenized elastic stiffness tensor of concrete $\mathbb{C}_{con}$ as

$$\boldsymbol{\Sigma}_{con} = \mathbb{C}_{con} : (\mathbf{E}_{con} - \mathbf{E}^{e}_{con}). \tag{9}$$

The homogenized stiffness tensor of the concrete is (Hill, 1963)

$$\mathbb{C}_{con} = f_{cp}\,\mathbb{C}_{cp} : \mathbb{A}_{cp} + f_{agg}\,\mathbb{C}_{agg} : \mathbb{A}_{agg}, \tag{10}$$

and its homogenized eigenstrain tensor is (Levin, 1967; Wang et al., 2017a)

$$\mathbf{E}^{e}_{con} = \mathbb{C}^{-1}_{con} : \left[f_{cp}\left(\mathbb{C}_{cp} : \boldsymbol{\varepsilon}^{e}_{cp}\right) : \mathbb{A}_{cp} + f_{agg}\left(\mathbb{C}_{agg} : \boldsymbol{\varepsilon}^{e}_{agg}\right) : \mathbb{A}_{agg}\right], \tag{11}$$

where f_{cp} and f_{agg}, $\mathbb{C}_{cp}$ and $\mathbb{C}_{agg}$, and $\mathbb{A}_{cp}$ and $\mathbb{A}_{agg}$ are the volume fractions, the elastic stiffness tensors, and the strain concentration tensors of the cement paste and the aggregates, respectively. The strain concentration tensors are estimated by using the Mori-Tanaka scheme (Mori and Tanaka, 1973; Benveniste, 1987):

$$\mathbb{A}_{k} = \left[\mathbb{I} + \mathbb{P} : (\mathbb{C}_{k} - \mathbb{C}_{cp})\right]^{-1} : \left\{ f_{cp}\mathbb{I} + f_{agg}\left[\mathbb{I} + \mathbb{P} : (\mathbb{C}_{agg} - \mathbb{C}_{cp})\right]^{-1} \right\}^{-1}, \tag{12}$$

with $k \in [cp, agg]$, where $\mathbb{I}$ is the symmetric fourth-order identity tensor, and $\mathbb{P}$ is the fourth-order Hill tensor, accounting for the spherical shape of the aggregates embedded in the cement paste matrix.

In order to quantify the thermal expansion coefficient of the concrete, α_{con}, the representative volume of concrete is considered to deform freely, resulting in the vanishing of the macroscopic stress tensor, i.e., $\boldsymbol{\Sigma}_{con} = 0$. Consideration of this expression in Eq. (9) indicates that the macroscopic eigenstrains are equal to the total macroscopic strains: $\mathbf{E}^{e}_{con} = \mathbf{E}_{con}$. Thus,

$$\mathbf{E}^{e}_{con} = \alpha_{con}\,\Delta T\,\mathbf{1}. \tag{13}$$

The sought expression for α_{con} is obtained by inserting Eqs. (8) and (10) into Eq. (11) and substituting the resulting expression into Eq. (13). After division by ΔT (Wang et al., 2017a, 2018) and re-arrangement of terms, the following expression for α_{con} is obtained:

$$\alpha_{con} = \frac{1}{3}\left\{\mathbb{C}^{-1}_{con} : \left[\alpha_{cp} f_{cp}(\mathbb{C}_{cp} : \mathbf{1}) : \mathbb{A}_{cp} + \alpha_{agg} f_{agg}(\mathbb{C}_{agg} : \mathbf{1}) : \mathbb{A}_{agg}\right]\right\} : \mathbf{1}. \tag{14}$$

Eq. (14) indicates that the homogenized thermal expansion coefficient of concrete is not only a function of the thermal expansion coefficients and the volume fractions of the cement paste and the aggregates, but also of the stiffness contrast between these two constituents.

The thermal expansion coefficient of the concrete of the HZMB is computed according to (14). Therein, the thermal expansion coefficient of the quartz aggregates is set equal to $11 \cdot 10^{-6}/^{\circ}\mathrm{C}$, see (Emanuel and Hulsey, 1977) and Table 7. As for the cement paste, a relative humidity amounting to 80% is considered as a typical value during regular service of the HZMB. The corresponding thermal expansion coefficient of the cement paste is equal to $18 \cdot 10^{-6}/^{\circ}\mathrm{C}$, see (Emanuel and Hulsey, 1977) and Table 7. The homogenized stiffness values of the concrete are obtained from the multiscale model of Königsberger et al. (2018), see Fig. 5 and Table 7. The homogenized thermo-elastic properties of concrete serve as input for the macroscopic thermo-mechanical analysis of steel-reinforced concrete beams.

4.2 Macroscopic thermo-mechanical analysis of reinforced concrete beams subjected to sudden heating

A simplified linear-elastic structural analysis is carried out. The overhead-slab of the segments of the immersed tunnel of the HZMB is idealized as a reinforced concrete beam (Fig. 8). The height of the beam is 150 cm. It is equal to the thickness of the overhead-slab of the immersed tunnel shown in Fig. 2. Four layers of rebars, with diameters of 32 mm, 36 mm, 36 mm, and 40 mm are considered, by comparing Fig. 8 with Fig. 2.

As for the mechanical boundary conditions, two bounding scenarios are investigated: one beam is simply supported and the other one is clamped at both extremities (Fig. 8). The real support conditions of the overhead-slab, which are monolithically connected to the rest of the tunnel segments, falls in between the two types of extreme boundary conditions.

As for the thermal boundary conditions, both beams are subjected to a uniform reference temperature, T_{ref}, in the initial configuration

$$T(y, t < 0) = T_{ref}. \tag{15}$$

At the time instant $t = 0$, the bottom surfaces of the beams are subjected to a sudden temperature increase up to the level T_{hot}, while the temperature at the top surfaces remains T_{ref}, i.e.

$$T\left(y = -\frac{h}{2}, t\right) = T_{hot}, \quad T\left(y = +\frac{h}{2}, t\right) = T_{ref}. \tag{16}$$

The four lateral surfaces of the beams are assumed to be thermally insulated. Thus, a problem of one-dimensional heat conduction from the bottom to the top of the beam is obtained. This problem is described by the following partial differential equation:

$$\frac{\partial T}{\partial t} - a\frac{\partial^2 T}{\partial y^2} = 0, \tag{17}$$

where a represents the thermal diffusivity of the concrete. The latter is assumed to be uniform in the entire volume of the steel-reinforced concrete beams. This is reasonable,

Table 7
Volume fractions, Young's modulus, shear modulus, and thermal expansion coefficient of the cement paste and the aggregates of the concrete used for the segments of the immersed tunnel of the Hong Kong-Zhuhai-Macao Bridge, and corresponding thermo-mechanical properties of the homogenized concrete and of steel.

Material	Volume fraction [–]	Young's modulus [GPa]	Shear modulus [GPa]	Thermal expansion coefficient [10^{-6}/°C]
Aggregate	0.70	60.00	23.0	11.00
Cement paste	0.30	22.34	9.1	18.00
Concrete	–	43.30	17.0	12.55
Steel	–	200.00	76.9	12.00

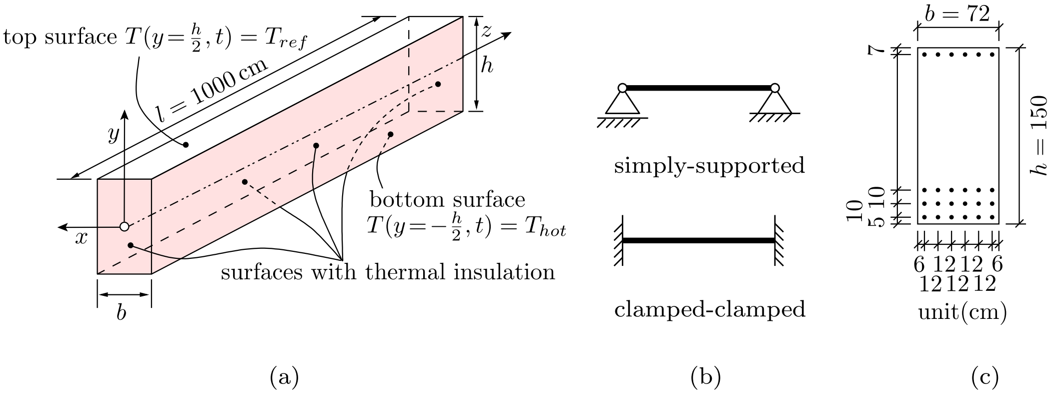

Fig. 8. Reinforced concrete beams (a) subjected to sudden heating at their bottom surfaces, (b) with two types of mechanical boundary conditions, and (c) the dimensions of the cross-section and the properties of the steel reinforcements are inspired by the overhead-slab of the segments of the immersed tunnel of the Hong Kong-Zhuhai-Macao Bridge, see Fig. 2.

because the influence of the rebars on the temperature distribution inside the cross-sections of the steel-reinforced concrete beams is insignificant (Kodur and Dwaikat, 2008; Lie and Erwin, 1993).

The initial condition (15) and the boundary conditions (16) describe a *jump* in temperature at the bottom of the beam at the time instant $t=0$. For this case, an analytical solution for the transient temperature problem is available. Before describing it in more detail, it is worth mentioning that in various international standards for the design of tunnels in the context of fire-resistance, *time variant* temperature boundary conditions are also suggested. They read as $T\left(y=-\frac{h}{2},t\right)=T_{hot}(t)$, whereby $T_{hot}(t)$ is a known function, see, e.g. (Ingason, 2004). In such a case, a *numerical* computation of the time variant temperature field is required.

The analytical solution of the heat conduction problem, defined by Eqs. (15)–(17), reads as (Binder et al., 2018; Wang et al., 2017a)

$$\frac{T-T_{hot}}{T_{ref}-T_{hot}}=\left(\frac{1}{2}+\frac{y}{h}\right)-\sum_{n=1}^{\infty}\frac{(-1)^{n-1}}{n\pi}\sin\left(2n\pi\frac{y}{h}\right)\exp\left[-(2n\pi)^2\frac{at}{h^2}\right]+\sum_{n=1}^{\infty}\frac{2(-1)^{n-1}}{(2n-1)\pi}\cos\left[(2n-1)\pi\frac{y}{h}\right]\exp\left[-(2n-1)^2\pi^2\frac{at}{h^2}\right]. \tag{18}$$

According to Eq. (18), the temperature distribution is a function of y/h and of at/h^2 (Fig. 9). During the initial phase of instationary heat conduction, right after the application of the sudden temperature change, the temperature is varying nonlinearly along the height of the beam. Large temperature gradients are observed in the vicinity of the thermally loaded bottom surface. A linear distribution of the temperature field and, thus, steady-state heat conduction, is reached at the dimensionless time instant $at/h^2=1$.

Three-dimensional Finite Element simulations are carried out to compute the macroscopic thermal stresses of the steel-reinforced concrete beams, resulting from the temperature distributions depicted in Fig. 9. As regards the input values for these computations, the material properties are taken from Table 7. The numerical values for the beam dimensions and the temperatures are chosen as $l=1000$ cm, $b=72$ cm, $h=150$ cm, $T_{ref}=20\,°\mathrm{C}$ and

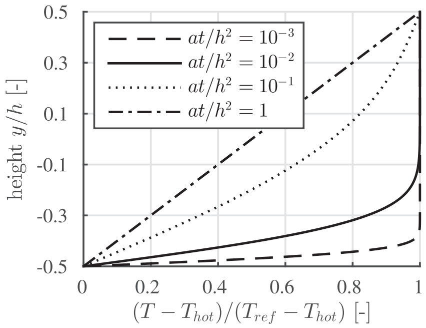

Fig. 9. Temperature distribution along the height of the investigated steel-reinforced concrete beams as a function of the dimensionless time at/h^2.

$T_{hot} = 100\,^{\circ}\mathrm{C}$. The latter choice refers to a moderate “fire load”. Still, the sudden temperature increase by 80 °C is well suited for the assessment of the potential added value of multiscale analysis. The thermal diffusivity of the concrete amounts to $a = 4.73 \cdot 10^{-7}\ \mathrm{m}^2/\mathrm{s}$ (Wang et al., 2017a). Therefore, the dimensionless time instants $at/h^2 = 10^{-3}$ and $at/h^2 = 10^{-2}$ are approximately equal to 1.3 hours and 13 hours after the sudden temperature increase.

The distributions of the dominating axial normal stresses, $\Sigma_{zz}(y)$, experienced by the concrete along the y-axis at the midspans of the simply-supported and clamped-clamped reinforced concrete beams are shown in Fig. 10. At the dimensionless time instant $at/h^2 = 10^{-3}$, the restrained thermal strains result in compressive axial stresses close to the bottom of the beams. Independent of the support conditions, these stresses are of similar magnitude, see the dashed graphs in Fig. 10.

As for the simply-supported beam, in the absence of mechanical loads, the overall equilibrium of the structure implies the vanishing of the stress resultants, i.e.,

$$N = \int_{-h/2}^{+h/2} \Sigma_{zz}\,\mathrm{d}A = 0, \qquad M = \int_{-h/2}^{+h/2} \Sigma_{zz} y\,\mathrm{d}A = 0. \qquad (19)$$

Because of the vanishing normal force and the heating-induced compressive axial stresses close to the bottom of the beam must be balanced by tensile axial stresses. The axial stresses develop in the central region of the beam, see Fig. 10(a). Because of the vanishing bending moment, equilibrium requires also compressive axial stresses close to the top of the beam, see Fig. 10(a). With increasing time, the axial normal stresses gradually decrease as the heat conduction approaches the stationary solution associated with a linear temperature distribution (Fig. 10(a)). Although the simply-supported beam is statically *determinate*, small axial normal stresses remain in the final configuration. This is the consequence of the small difference in the thermal expansion coefficients of the concrete and steel (Table 7).

As for the clamped-clamped beam, the nonlinear stress profile progressively turns into a linear stress distribution. The latter is reached in the stationary regime, see Fig. 10(b). The stress resultants, i.e., the compressive normal force and the negative bending moment, increase progressively because of the statically *indeterminate* support conditions. The steel reinforcement almost has no influence on the thermal stresses, because the thermal expansion coefficient of the concrete is very similar to that of steel.

While the axial stresses dominate the stress components, triaxial principal stress states prevail along the y-axis at the midspans of the two analyzed beams. Figure 11 contains illustrations of the stress states referring to the dimensionless time instant $at/h^2 = 10^{-2}$. The principal normal stresses in the x- and the y-direction result from the incompatibility of the macroscopic thermal eigenstrain fields, which is associated with the nonlinear temperature distribution (Wang et al., 2017a, 2018). As for the simply-supported beam, it is remarkable that triaxial *tensile* stress states are obtained in the region below the middle of the axis of the beam. Corresponding stress magnitudes amount up to 10 MPa. This is larger than the tensile strength of the concrete used for the immersed tunnel of the HZMB. While this clearly underlines the risk of cracking, a more detailed analysis of the expected failure mode is carried out in the context of the following multiscale analysis.

4.3 Top-down quantification of the average stresses of the cement paste matrix and the aggregates, at the time instant $at/h^2 = 10^{-2}$

In the context of a classical macroscopic mode of analysis, the stress distributions depicted in Figs. 10 and 11 would be the final result. The present multiscale structural analysis continues with top-down quantification of the average stresses in the cement paste matrix and the aggregates.

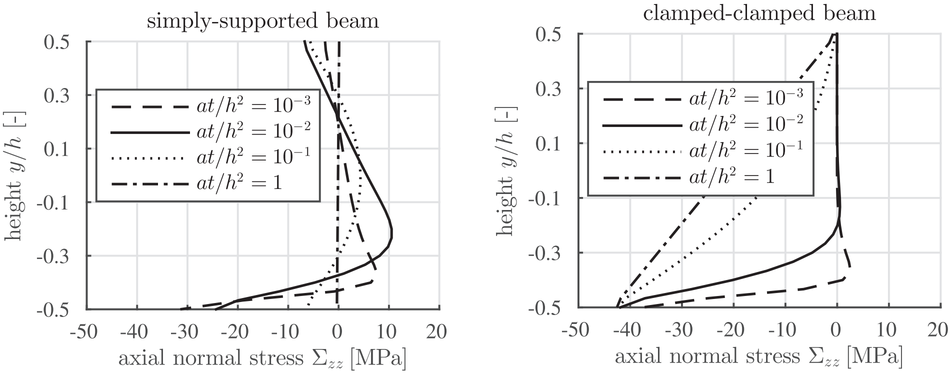

(a) (b)

Fig. 10. Macroscopic axial normal stress in the concrete, resulting from the temperature distributions depicted in Fig. 9, along the height of the analyzed steel-reinforced concrete beams as a function of the dimensionless time at/h^2: (a) simply-supported beam and (b) clamped-clamped beam.

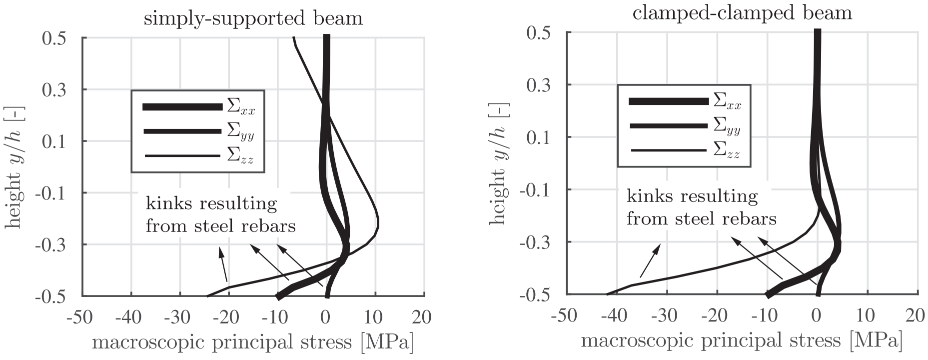

(a)

(b)

Fig. 11. Triaxial macroscopic stress states, experienced by concrete at the dimensionless time instant $at/h^2 = 10^{-2}$, as a function of the position along the y-axis: (a) simply-supported beam and (b) clamped-clamped beam; as for the underlying temperature distribution, see Fig. 9.

The *macroscopic* temperature and stress distributions, depicted in Figs. 9 and 11, represent input for the computation of *microscopic* stress distributions in the cement paste matrix and the aggregates. This requires computation of (i) the microscopic eigenstrains of both the cement paste and the aggregates, based on Eq. (8), (ii) the macroscopic eigenstrains of the concrete, based on Eq. (11), and (iii) the total macroscopic strains of the concrete, based on Eq. (9). With these quantities at hand, the microscopic strains of the cement paste and the aggregates are quantified as (Zaoui, 2002)

$$\begin{aligned}\boldsymbol{\varepsilon}_k = {} & [\mathbb{I} + \mathbb{P} : (\mathbb{C}_k - \mathbb{C}_{cp})] : [\mathbf{E}_\infty + \mathbb{P} : (\mathbb{C}_k : \boldsymbol{\varepsilon}^e_k - \mathbb{C}_{cp} \\ & : \boldsymbol{\varepsilon}^e_{cp})], \quad k \in [cp, agg],\end{aligned} \tag{20}$$

with $\mathbf{E}_\infty$ reading as (Zaoui, 2002)

$$\begin{aligned}\mathbf{E}_\infty = {} & \left\{ f_{cp}\mathbb{I} + f_{agg}\left[\mathbb{I} + \mathbb{P} : (\mathbb{C}_{agg} - \mathbb{C}_{cp})\right]^{-1} \right\}^{-1} \\ & : \left\{ \mathbf{E}_{con} + f_{agg}\left[\mathbb{I} + \mathbb{P} : (\mathbb{C}_{agg} - \mathbb{C}_{cp})\right]^{-1} \right. \\ & \left. : \mathbb{P} : (-\mathbb{C}_{agg} : \boldsymbol{\varepsilon}^e_{agg} + \mathbb{C}_{cp} : \boldsymbol{\varepsilon}^e_{cp}) \right\}.\end{aligned} \tag{21}$$

The microscopic stresses of the cement paste and the aggregates, $\boldsymbol{\sigma}_k$, with $k \in [cp, agg]$ follow from the generalized Hooke's law:

$$\boldsymbol{\sigma}_k = \mathbb{C}_k : (\boldsymbol{\varepsilon}_k - \boldsymbol{\varepsilon}^e_k), \quad k \in [cp, agg]. \tag{22}$$

Finally, it is worth emphasizing that the microscopic stresses in the cement paste and the aggregates satisfy the stress average rule:

$$\boldsymbol{\Sigma}_{con} = f_{cp}\boldsymbol{\sigma}_{cp} + f_{agg}\boldsymbol{\sigma}_{agg}. \tag{23}$$

As for the concrete of the tunnel, $f_{cp} = 0.30$ and $f_{agg} = 0.70$.

Results from top-down stress concentration are discussed for the dimensionless time instants $at/h^2 = 10^{-2}$, see Fig. 12. The analyzed thermo-mechanical problem involves two types of microstructural stress fluctuations discussed in the following two paragraphs.

The "thermal" contribution to microstructural stress fluctuations refers to the mismatch of the microscopic thermal expansion coefficients of the cement paste and the aggregates. As for the analyzed *increase* in the temperature, larger expansive eigenstrains develop in the cement paste and smaller ones in the aggregates. The compatibility of the total microscopic strain field requires stress-related ("mechanical") strains, which are related, on average, to compressive stresses in the cement paste and to tensile stresses in the aggregates. This is particularly visible when comparing the macrostress component $\Sigma_{con,yy}$ with the microstress components $\sigma_{cp,yy}$ and $\sigma_{agg,yy}$ at the bottom of the beams, where $\Sigma_{con,yy} = 0$, see Figs. 12(c) and (d). In addition, the described "thermal" contribution explains why the cement paste exhibits smaller stresses and the aggregates larger stresses compared to the macroscopic stresses of the concrete, see all Figs. 12(a)–(f).

The "mechanical" contribution to microstructural stress fluctuations results from macro-to-micro stress concentration, governed by the stiffness contrast between the cement paste and the aggregates. The aggregates, representing the stiffer components of the statically indeterminate microstructure of concrete, "attract" a larger share of the macroscopic stresses. The less stiff cement paste "attracts" a smaller share of the macroscopic stresses. Therefore, the stress concentration results in larger stress levels in the aggregates and smaller stress levels in the cement paste, relative to the stress level at the macroscopic scale of concrete.

The described "thermal" and "mechanical" effects *counteract* each other in regions of the beams, where the *heated* concrete is subjected to macroscopic *compressive* stresses. This is particularly visible in Figs. 12(e)–(f), close to the bottom of the cross-section, where the two effects almost cancel each other, such that no significant stress fluctuations are obtained.

The described "thermal" and "mechanical" effects *augment* each other in regions of the beams, where the *heated* concrete is subjected to macroscopic *tensile* stresses. This results in quite significant stress fluctuations, see the

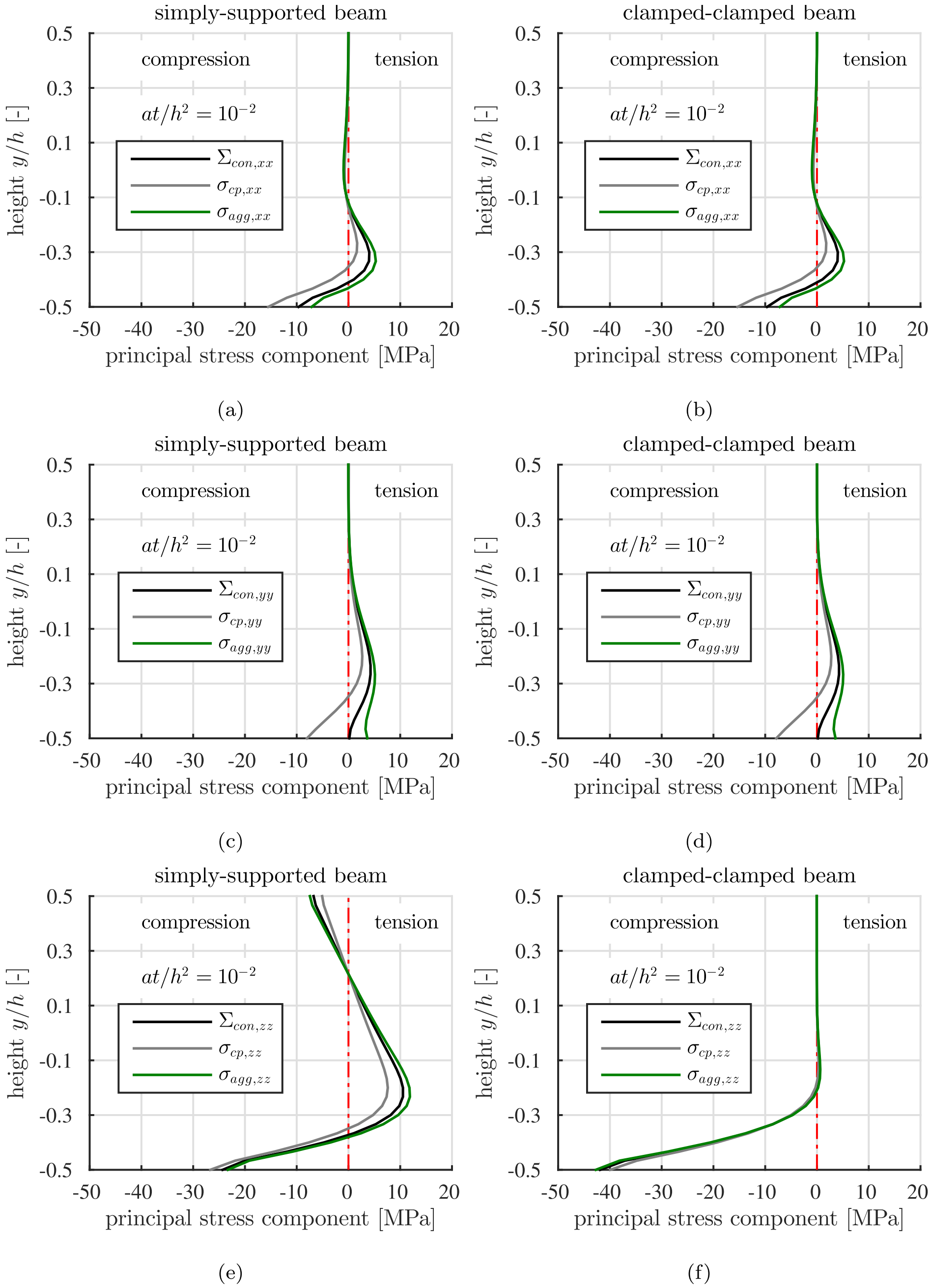

(a) (b) (c) (d) (e) (f)

Fig. 12. Macroscopic stresses in the concrete and microscopic stresses in the cement paste and the aggregates of the simply-supported beam, see (a), (c), and (e) and of the clamped-clamped beam, see (b), (d), and (f) at the dimensionless time instant $at/h^2 = 10^{-2}$: (a) and (b) refer to the principal stress acting in the x-direction, (c) and (d) to the dominating principal stress acting in the y-direction, and (e) and (f) to the principal stress acting in the z-direction.

regions exhibiting tensile stresses in Figs. 12(a)–(f). There, the microscopic stresses of the cement paste are significantly smaller than the ones of the aggregates. Therefore, significant tensile stresses must be transmitted across the "interfacial transition zones" between the cement paste and the aggregates. These tensile stresses further increase the cracking risk in form of debonding, as has been investigated by Königsberger et al. (2014a,b).

Comparing simulation results obtained with the two different types of boundary conditions, it allows for assessing the probability of tension-induced damage of the segments of the tunnel. This probability reduces with increasing macrostructural restraints that are counteracting the free expansion of the overhead-slab of the tunnel segments. Given that these segments are produced monolithically and contain many steel rebars (Fig. 2), a rather localized heating of the overhead-slab will activate in-plane compressive normal forces, because the heated part of the segment cannot expand freely. Compression will effectively counteract the development of tensile stresses. Therefore, it is concluded that the statically indeterminate nature of the segments of the tunnel, representing closed frame structures, is beneficial to preventing tension-induced damage inside the cross-sections.

4.4 Superposition of stresses resulting from dead load and water pressure

Because the presented analysis of thermal stresses was carried out in the framework of *linear* multiscale thermoelasticity, it is straightforward to superimpose other load cases, such as dead load and water pressure. The latter two types of loading were analyzed using Finite Element simulations by Guo et al. (2016). They focused on a tunnel segment, the top of which is located 33.44 m below the sea level. In addition, the height of the overburden of the analyzed segment by backfill material is equal to 21.79 m. The Finite Element simulations showed that the absolute values of the compressive normal stresses prevailing in the lowest third of the cross-section at midspan of the overhead-slab are smaller than 1 MPa, see Fig. 7 of (Guo et al., 2016). This shows that compressive stresses resulting from dead load and water pressure cannot significantly counteract the tensile stresses quantified in the present study. Thus, the presented discussion of thermal stresses and the corresponding conclusions regarding the risk of cracking of concrete in the lowest third of the cross-section at midspan of the overhead-slab remain valid, even if the load cases “dead load” and “water pressure” are superimposed.

5 Summary and conclusions

As for the high-dynamic strength of concrete specimens, the presented study has led to the following conclusions, based on the obtained numerical results:

- The *DIF* expression according to the combination of Eqs. (1) and (2) is capable of explaining the experimental data published by Zhang et al. (2009), who tested two groups of mortar specimens of *different size*. This indicates that the high-dynamic strength values of concrete depend on the structural dimensions of the tested specimens.
- The *DIF* expression according to the combination of Eqs. (1) and (2) was evaluated for the concrete of the HZMB. The multiscale model of Königsberger et al. (2018) delivered reliable estimates of the evolution of the stiffness and the quasi-static strength, accompanying the progressive hardening of concrete at material ages greater than 28 days. It was found that the *DIF* values *decrease* and that the high-dynamic strength values *increase* with increasing age of concrete, because concrete hardening results in a significant increase in the quasi-static strength and a much less significant increase in the elastic stiffness.
- As for a vehicle impact on the tunnel wall, it is concluded that irrespective of how short the stress pulse lasts and how fast the stress pulse is applied, the tunnel lining will be damaged provided that the stress pulse exceeds the quasi-static strength, because high-dynamic strengthening refers to an increase in the external loading *during* crack propagation, and crack propagation starts, once the *quasi-static* strength is reached. Therefore, it is recommended to carry out a careful inspection even after non-catastrophic impact events.

As for the thermal stresses of steel-reinforced concrete structures, the present study has led to the following conclusions, based on the obtained numerical results:

- Steel-reinforced concrete beams, which are structural approximations of the overhead-slab of the segments of the immersed tunnel of the HZMB, were analyzed. It was assumed that the beams are exposed to sudden heating at their bottom surfaces. The results from macroscopic analysis suggest that the macroscopic thermal stresses are governed by kinematic constraints. These result from (i) the support conditions at the extremities of the analyzed beams and (ii) the incompatibility of concrete-related eigenstrains resulting from *nonlinear* temperature distributions along the height of the beams, which are observed during *instationary* heat conduction. The steel reinforcement, in turn, was shown to have less influence on the macroscopic thermal stresses, because the thermal expansion coefficients of steel and concrete are quite similar.
- Multiscale postprocessing of the macroscopic thermomechanical analysis has shown that macroscopic stresses experienced by concrete differ, in general, from the microscopic stresses experienced by the cement paste and the aggregates. The microstructural stress fluctuations result from two effects: one is of thermal nature, and the other of mechanical origin. On the one hand, inhomogeneous thermal expansion of different microstructural constituents results in incompatible thermal eigenstrain fields. The compatibility of the total strain field requires mechanical (stress-related) strains. On the other hand, the stress concentration of macroscopic stress states into the microstructural constituents is governed by stiffness contrasts. The stress concentration into stiffer microstructural constituents is more pronounced than into less stiff constituents. In the analyzed problem, where a sudden temperature increase was investigated, the two stress fluctuation effects counteract each other in regions where concrete experiences compressive stresses, and they augment each other in regions where concrete experiences tensile stresses. This increases the risk of debonding in the “interfacial transition zones” between the cement paste matrix and the aggregates.
- As for a moderate fire resulting in a rather localized heating of the overhead-slab of the investigated tunnel segments, it is concluded that the layout of the segments in form of *closed* reinforced concrete cells is beneficial. The restraints counteracting the free in-plane deformation of the overhead slab are particularly effective in

preventing damage of concrete by means of debonding in the interfacial transition zones between the cement paste matrix and the aggregates.

The following added values were identified in the context of combining macroscopic modes of structural analysis with multiscale models of concrete.

- Modern multiscale models can be specified for any concrete mix of interest. They account, in a *customized* fashion, for the specific amounts of binder, water, and aggregates used for the production of the concrete.
- Validated multiscale models provide reliable predictions of the hardening-induced evolution of the mechanical properties of concrete. This is not only beneficial when it comes to the analysis of early-age structural behavior of shotcrete tunnel linings, such as those encountered in the New Austrian Tunneling Method (NATM), see, e.g., (Ullah et al., 2010, 2012, 2013), but also when considering that hardening of concrete continues progressively, rather than stopping abruptly, at a material age of 28 days, see Section 3.
- The combination of modern multiscale material models and classical modes of structural analysis is straightforward. This does *not necessarily* require full integration of multiscale models into structural simulation tools. In the present paper, this was demonstrated exemplarily. Both in Sections 3 and 4, bottom-up homogenization methods delivered input values for structural simulations, see also (Kalliauer et al., 2017) for a similar approach. In Section 4, top-down stress concentration methods were used for postprocessing macroscopic simulation results.

Thus, multiscale models for concrete have the potential to increase the “informative content” of structural simulations, as introduced philosophically by Popper (2014).

Acknowledgments

Financial support by the Austrian Science Fund (FWF), provided within project P 281 31-N32 “Bridging the Gap by Means of Multiscale Structural Analyses”, and interesting discussions with Mr. Rodrigo Díaz Flores (TU Wien), Dr. Wei Jiang (Tongji University), and Dr. Chong Li (Tongji University) are gratefully acknowledged. The first author also gratefully acknowledges financial support by the China Scholarship Council (CSC).

References

Acker, P. (2001). Micromechanical analysis of creep and shrinkage mechanisms. *Creep, shrinkage and durability mechanics of concrete and other quasi-brittle materials*. Cambridge, MA (pp. 15–25).

Bangert, F., Grasberger, S., Kuhl, D., & Meschke, G. (2003). Environmentally induced deterioration of concrete: Physical motivation and numerical modeling. *Engineering Fracture Mechanics, 70*(7), 891–910.

Bary, B., De Morais, M. V., Poyet, S., & Durand, S. (2012). Simulations of the thermo-hydro-mechanical behaviour of an annular reinforced concrete structure heated up to 200 °C. *Engineering Structures, 36*, 302–315.

Benveniste, Y. (1987). A new approach to the application of Mori-Tanaka’s theory in composite materials. *Mechanics of Materials, 6*(2), 147–157.

Bernard, O., Ulm, F.-J., & Lemarchand, E. (2003). A multiscale micromechanics-hydration model for the early-age elastic properties of cement-based materials. *Cement and Concrete Research, 33*, 1293–1309.

Binder, E., Mang, H., Yuan, Y., & Pichler, B. (2017). Impact and blast loads in tunneling: Does the strength of concrete indeed increase with the loading rate? In: *Proceedings of the IV international conference on computational methods in tunneling and subsurface engineering, University Innsbruck* (pp. 773–780).

Binder, E., Wang, H., Schlappal, T., Zhang, J., Yuan, Y., Pichler, B., & Mang, H. (2018). Bridging the gap between concrete microstructures and tunnel linings. In E. Oñate, D. Peric, E. de Souza Neto, & M. Chiumenti (Eds.), *Advances in computational plasticity* (pp. 23–44). Springer.

Chatterji, S., & Jeffery, J. (1966). Three-dimensional arrangement of hydration products in set cement paste. *Nature, 209*(5029), 1233–1234.

Dormieux, L., Kondo, D., & Ulm, F.-J. (2006). *Microporomechanics*. John Wiley & Sons.

Dvorak, G. J. (1992). Transformation field analysis of inelastic composite materials. *Proceedings of the Royal Society of London A: Mathematical, Physical and Engineering Sciences, 437*(1900), 311–327.

Emanuel, J. H., & Hulsey, J. L. (1977). Prediction of the thermal coefficient of expansion of concrete. *Journal Proceedings of the American Concrete Institute, 74*(4), 149–155.

European Committee for Standardization (2011). *Eurocode 2: Design of concrete structures – Part 1-1: General rules and rules for buildings*.

Feist, C., Aschaber, M., & Hofstetter, G. (2009). Numerical simulation of the load-carrying behavior of RC tunnel structures exposed to fire. *Finite Elements in Analysis and Design, 45*(12), 958–965.

Fischer, I., Pichler, B., Lach, E., Terner, C., Barraud, E., & Britz, F. (2014). Compressive strength of cement paste as a function of loading rate: Experiments and engineering mechanics analysis. *Cement and Concrete Research, 58*, 186–200.

Fu, Y., Wong, Y., Tang, C., & Poon, C. (2004a). Thermal induced stress and associated cracking in cement-based composite at elevated temperatures – Part I: Thermal cracking around single inclusion. *Cement and Concrete Composites, 26*(2), 99–111.

Fu, Y., Wong, Y., Tang, C., & Poon, C. (2004b). Thermal induced stress and associated cracking in cement-based composite at elevated temperatures – Part II: Thermal cracking around multiple inclusions. *Cement and Concrete Composites, 26*(2), 113–126.

Fu, Y., Wong, Y., Poon, C., & Tang, C. (2007). Numerical tests of thermal cracking induced by temperature gradient in cement-based composites under thermal loads. *Cement and Concrete Composites, 29*(2), 103–116.

Guo, J., Jiang, S., & Zhang, Z. (2016). Fire thermal stress and its damage to subsea immersed tunnel. *Procedia Engineering, 166*, 296–306.

Hansen, T. C. (1986). Physical structure of hardened cement paste. A classical approach. *Materials and Structures, 19*(6), 423–436.

Hellmich, C., & Mang, H. (2005). Shotcrete elasticity revisited in the framework of continuum micromechanics: From submicron to meter level. *Journal of Materials in Civil Engineering (ASCE), 17*(3), 246–256.

Hill, R. (1963). Elastic properties of reinforced solids. *Journal of Mechanics and Physics of Solids, 11*(5), 357–372.

Hu, Z.-N., Xie, Y.-L., & Wang, J. (2015). Challenges and strategies involved in designing and constructing a 6 km immersed tunnel: A case study of the Hong Kong–Zhuhai–Macao Bridge. *Tunnelling and Underground Space Technology, 50*, 171–177.

Ingason, H., Lönnermark, A. (2004). Recent achievements regarding measuring of time-heat and time-temperature development in tunnels. In: *1st International symposium on safe & reliable tunnels, Prague, Czech Republic* (pp. 4–6).

Irfan-ul-Hassan, M., Königsberger, M., Reihsner, R., Hellmich, C., & Pichler, B. (2017). How water-aggregate interactions affect concrete creep: A multiscale analysis. *Journal of Nanomehanics and Micromechanics (ASCE), 7*(4), 04017019.

Kalliauer, J., Schlappal, T., Vill, M., Mang, H., & Pichler, B. (2017). Bearing capacity of concrete hinges subjected to eccentric compression: Multiscale structural analysis of experiments. *Acta Mechanica*, 1–18.

Kodur, V., & Dwaikat, M. (2008). A numerical model for predicting the fire resistance of reinforced concrete beams. *Cement and Concrete Composites, 30*(5), 431–443.

Königsberger, M., Pichler, B., & Hellmich, C. (2014a). Micromechanics of ITZ-aggregate interaction in concrete Part I: Stress concentration. *Journal of the American Ceramic Society, 97*(2), 535–542.

Königsberger, M., Pichler, B., & Hellmich, C. (2014b). Micromechanics of ITZ-aggregate interaction in concrete Part II: Strength upscaling. *Journal of the American Ceramic Society, 97*(2), 543–551.

Königsberger, M., Irfan-ul-Hassan, M., Pichler, B., & Hellmich, C. (2016). Downscaling-based identification of non-aging power-law creep of cement hydrates. *Journal of Engineering Mechanics (ASCE), 142*(12), 04016106.

Königsberger, M., Hlobil, M., Delsaute, B., Staquet, S., Hellmich, C., & Pichler, B. (2018). Hydrate failure in ITZ governs concrete strength: A micro-to-macro validated engineering mechanics model. *Cement and Concrete Research, 103*, 77–94.

Kühn, T., Steinke, C., Sile, Z., Zreid, I., Kaliske, M., & Curbach, M. (2016). Dynamische Eigenschaften von Beton im Experiment und in der Simulation (Dynamic properties of concrete in experiments and simulations). *Beton- und Stahlbetonbau, 111*(1), 41–50.

Levin, V. (1967). Coefficients of temperature expansion of heterogeneous materials. *Mechanics of Solids, 2*, 88–94.

Lie, T., & Erwin, R. (1993). Method to calculate the fire resistance of reinforced concrete columns with rectangular cross section. *ACI Structural Journal, 90*(1), 52–60.

Mori, T., & Tanaka, K. (1973). Average stress in matrix and average elastic energy of materials with misfitting inclusions. *Acta Metallurgica, 21*(5), 571–574.

Pichler, B., & Hellmich, C. (2010). Estimation of influence tensors for eigenstressed multiphase elastic media with nonaligned inclusion phases of arbitrary ellipsoidal shape. *Journal of Engineering Mechanics, 136*(8), 1043–1053.

Popper, K. (2014). *Conjectures and refutations: The growth of scientific knowledge*. Routledge.

Powers, T. C., & Brownyard, T. L. (1946). Studies of the physical properties of hardened Portland cement paste. *Journal of the American Concrete Institute, 18*, 101–132.

Sarris, E., & Constantinides, G. (2013). Finite Element modeling of nanoindentation on C–S–H: Effect of pile-up and contact friction. *Cement and Concrete Composites, 36*, 78–84.

Taerwe, L., & Matthys, S. (2013). *Fib model code for concrete structures 2010*. Ernst & Sohn, Wiley.

Tai, Y. (2009). Uniaxial compression tests at various loading rates for reactive powder concrete. *Theoretical and Applied Fracture Mechanics, 52*(1), 14–21.

Ullah, S., Pichler, B., Scheiner, S., & Hellmich, C. (2010). Shell-specific interpolation of measured 3D displacements, for micromechanics-based rapid safety assessment of shotcrete tunnels. *Computer Modeling in Engineering and Sciences (CMES), 57*(3), 279–315.

Ullah, S., Pichler, B., Scheiner, S., & Hellmich, C. (2012). Influence of shotcrete composition on load-level estimation in NATM-tunnel shells: Micromechanics-based sensitivity analyses. *International Journal for Numerical and Analytical Methods in Geomechanics, 36*(9), 1151–1180.

Ullah, S., Pichler, B., & Hellmich, C. (2013). Modeling ground-shell contact forces in NATM tunneling based on three-dimensional displacement measurements. *Journal of Geotechnical and Geoenvironmental Engineering, 139*(3), 444–457.

Ulm, F.-J., & Coussy, O. (1995). Modeling of thermochemomechanical couplings of concrete at early ages. *Journal of Engineering Mechanics, 121*(7), 785–794.

Walker, H. N., Lane, D. S., & Stutzman, P. E. (2006). *Petrographic methods of examining hardened concrete: A petrographic manual*. Tech. rep. FHWA-HRT-04-150. McLean, Virginia: U.S. Department of Transportation, Federal Highway Administration, Research and Development, Turner-Fairbanks Highway Research Center.

Wang, H., Ausweger, M., Mang, H., Yuan, Y., & Pichler, B. (2017a). Multiscale quantification of thermal stresses in concrete linings resulting from accidental sudden heating or cooling. In: *Proceedings of the IV international conference on computational methods in tunneling and subsurface engineering, Innsbruck, Austria* (pp. 781–788).

Wang, H., Mang, H., Yuan, Y., & Pichler, B. (2017b). Microporomechanical modeling of thermal expansion of cement pastes. In: *Poromechanics 2017 – Proceedings of the 6th biot conference on poromechanics, Paris, France* (pp. 746–753).

Wang, H., Mang, H., Yuan, Y., & Pichler, B. (2018). Multiscale quantification of thermal expansion of concrete and thermal stresses of concrete structures. In *Computational modelling of concrete structures: Proceedings of the conference on computational modelling of concrete and concrete structures (EURO-C 2018)* (pp. 257–264). Bad Hofgastein, Austria: CRC Press.

Wang, H., Hellmich, C., Yuan, Y., Mang, H., & Pichler, B. (submitted for publication). May reversible water uptake/release by hydrates explain the thermal expansion of cement paste? – Arguments from inverse multiscale analysis. *Cement and Concrete Research*.

Zaoui, A. (2002). Continuum micromechanics: Survey. *Journal of Engineering Mechanics (ASCE), 128*(8), 808–816.

Zhang, M., Wu, H., Li, Q., & Huang, F. (2009). Further investigation on the dynamic compressive strength enhancement of concrete-like materials based on split Hopkinson pressure bar tests. Part I: Experiments. *International Journal of Impact Engineering, 36*(12), 1327–1334.

Zhao, J., Zheng, J. J., Peng, G. F., & van Breugel, K. (2014). A meso-level investigation into the explosive spalling mechanism of high-performance concrete under fire exposure. *Cement and Concrete Research, 65*, 64–75.